

Article

# Nano-Crystalline $\text{Li}_{1.2}\text{Mn}_{0.6}\text{Ni}_{0.2}\text{O}_2$ Prepared via Amorphous Complex Precursor and Its Electrochemical Performances as Cathode Material for Lithium-Ion Batteries

Xiangming He <sup>1,2</sup>, Jixian Wang <sup>1</sup>, Li Wang <sup>1,3,\*</sup> and Jianjun Li <sup>1</sup>

<sup>1</sup> Institute of Nuclear & New Energy Technology, Tsinghua University, Beijing 100084, China; hexm@tsinghua.edu.cn (X.H.); wangjixian520@hotmail.com (J.W.); leejj@mail.tsinghua.edu.cn (J.L.)

<sup>2</sup> State Key Laboratory of Automotive Safety and Energy, Tsinghua University, Beijing 100084, China

<sup>3</sup> State Key Laboratory of New Ceramic and Fine Processing, Tsinghua University, Beijing 100084, China

\* Correspondence: wang-l@tsinghua.edu.cn; Tel.: +86-10-8979-6073; Fax: +86-10-8979-6031

Academic Editor: Martin Wilkening

Received: 17 May 2016; Accepted: 1 August 2016; Published: 5 August 2016

**Abstract:** An amorphous complex precursor with uniform Mn/Ni cation distribution is attempted for preparing a nano-structured layered Li-rich oxide ( $\text{Li}_{1.2}\text{Mn}_{0.6}\text{Ni}_{0.2}\text{O}_2$ ) cathode material, using diethylenetriaminepentaacetic acid (DTPA) as a chelating agent. The materials are characterized by powder X-ray diffraction (XRD), scanning electron microscopy (SEM), transmission electron microscopy (TEM), and electrochemical tests. The crystal structure of Li-rich materials is found to be closely related to synthesis temperature. As-obtained nano materials sintered at 850 °C for 10 h show an average size of 200 nm with a single crystal phase and good crystallinity. At a current density of 20  $\text{mA}\cdot\text{g}^{-1}$ , the specific discharge capacity reaches 221  $\text{mAh}\cdot\text{g}^{-1}$  for the first cycle and the capacity retention is 81% over 50 cycles. Even at a current density of 1000  $\text{mA}\cdot\text{g}^{-1}$ , the capacity is as high as 118  $\text{mAh}\cdot\text{g}^{-1}$ . The enhanced rate capability can be ascribed to the nano-sized morphology and good crystal structure.

**Keywords:** amorphous complex; nanoparticles; rate capability; Li-rich oxide; Lithium ion batteries

## 1. Introduction

Lithium-ion batteries are considered as a potential candidate for the next generation of energy storage system [1–4]. With the rapid development of the hybrid electric vehicle (HEV) and plug-in hybrid electric vehicle (PHEV), new battery chemistry with higher energy density, longer calendar life, higher reliability, and lower cost attracts increasing attention [5]. Layered  $\text{LiCoO}_2$  cathode material suffers from high cost, poor safety, and limited cycling life. Spinel  $\text{LiMn}_2\text{O}_4$  and olivine  $\text{LiFePO}_4$  are relatively safe, and are proved to be applicable for electric buses, while their application in passenger cars are debatable due to their low energy densities [3,6,7]. Layered Li-rich oxides with a formula of  $\text{Li}[\text{Li}_{(1/3-2x/3)}\text{Mn}_{(2/3-x/3)}\text{M}_x]\text{O}_2$  (M refers to Ni, Co, Mn, etc.) are regarded as promising candidates for the next generation of cathode materials due to their high capacity (200–300  $\text{mAh}\cdot\text{g}^{-1}$ , depending on x), high operating voltage (that is higher than 3.5 V vs.  $\text{Li}^+/\text{Li}$ ), better safety, and reduced cost [8–12].

Despite delivering high capacity, layered Li-rich oxide materials suffer from voltage fading and poor rate capability [13–15], and their electrochemical performances are sensitive to the synthesis method and condition [13,16–18]. The layered-to-spinel transformation has been proposed to account for the capacity fading and poor rate performance [13,16–20]. However, the structure complexity of layered Li-rich materials has not been fully understood until now. Dahn et al. considered it as solid solution with long-range order in transition metal layer [21], while Thackeray et al. yielded a composite

structure with domains only having short-range order [22]. Besides, Manthiram et al. investigated the effect of synthesis conditions on structure and electrochemical properties and reported the presence of a C2/m and R-3m two-phase mixture for samples synthesized at 1000 °C [23]. In the previous reports, many methods, including solid state method [24], sol-gel method [25], hydrothermal method [26], and combustion method [27] have been attempted to achieve Li-rich materials. To minimize layered Li-rich oxide primary particles to nano-size is generally considered to be necessary for achieving acceptable electrochemical performance [28], which means a short Li<sup>+</sup> diffusion pathway and a large contact area between electrode and electrolyte [29]. It has also been accepted that different synthesis strategies show different controllability in primary particle size and morphology [24,25,30]. In addition, element segregation at particle surface was reported as being possibly responsible for performance variation of nano-size layered Li-rich oxides. Uniform distributions of the Ni element at atomic level are reported to contribute to slow voltage fading, as Zheng et al. found in Li[Li<sub>0.2</sub>Ni<sub>0.2</sub>Mn<sub>0.6</sub>]O<sub>2</sub> prepared by a hydrothermal assisted sol-gel method [31]. Furthermore, Gu et al. discovered that Ni ions preferred to be segregated near the surface of Li[Li<sub>0.2</sub>Ni<sub>0.2</sub>Mn<sub>0.6</sub>]O<sub>2</sub> particles during high temperature sintering, which may have negative effects on cycling stability and rate capability of the cathode materials [32–34]. They found that nanoscale segregation driven by thermodynamic force was not only in Li[Li<sub>0.2</sub>Ni<sub>0.2</sub>Mn<sub>0.6</sub>]O<sub>2</sub> materials prepared by a co-precipitation method, but also in samples prepared using hydrothermal and sol-gel methods. Given that all of these syntheses employed annealing treatments, to further understand the thermal stability of the nano-crystal Li[Li<sub>0.2</sub>Ni<sub>0.2</sub>Mn<sub>0.6</sub>]O<sub>2</sub> may deliver some insightful information.

The amorphous complex method is of great advantage in the synthesis of composite oxides in terms of small particle size, high crystallinity, and high phase purity at a low calcination temperature [35–37]. Chelating agents such as glycine have been reported to be used in the synthesis of layered LiNi<sub>0.5</sub>Mn<sub>0.5</sub>O<sub>2</sub> oxide, but the decomposition of the precursor and formation of preliminary LiNi<sub>0.5</sub>Mn<sub>0.5</sub>O<sub>2</sub> oxide are clearly two separate processes, which might cause nonuniform cation diffusion and cation segregation during solid state reaction processes [38]. Diethylenetriaminepentaacetic acid (DTPA) is a kind of polynuclear complex, which has been reported to be efficient in synthesizing uniform composite oxide nano-crystalline even at low temperatures [37,39–41]. In previous researches using DTPA as a chelating agent, decomposition of the precursor and formation of preliminary oxide particles always occur nearly simultaneously [37,40], which may avoid nonuniform solid diffusion during crystalline formation. Therefore, here we used a DTPA-based amorphous complex method to prepare nano-sized Li<sub>1.2</sub>Mn<sub>0.6</sub>Ni<sub>0.2</sub>O<sub>2</sub> materials with uniform composition from low to high temperatures. Better understanding of the effect that temperature has on crystalline structure features, crystallization variation, and crystalline thermal stability of Li-rich materials, as well as the contribution of these characteristics to the electrochemical performances, are expected to be obtained through this study.

## 2. Experimental Section

### 2.1. Preparation of Li<sub>1.2</sub>Mn<sub>0.6</sub>Ni<sub>0.2</sub>O<sub>2</sub> Nanoparticles

First, a certain amount of DTPA was dissolved in 150 mL deionized water under continuous heating and magnetic stirring for 1 h to form solution A. Later, LiCO<sub>3</sub>, MnCO<sub>3</sub>, and NiCO<sub>3</sub>·2Ni(OH)<sub>2</sub>·4H<sub>2</sub>O powder were added into solution A in stoichiometric ratio. After a 2 h reaction, the obtained solution was transferred in to a Teflon-lined stainless steel autoclave and heated at 80 °C for 12 h. A clear solution was formed. This solution was evaporated to form a precursor. The as-obtained precursor was heated at 650, 750, 850, and 950 °C for 10 h, and cooled down naturally to room temperature.

### 2.2. Materials Characterization

Thermo-gravimetric (TG) analysis and differential scanning calorimetric (DSC) analyses were performed with PerkinElmer Diamond (NETZSCHSTA 409 PC/PG, Netzsch, Selb, Germany).

Crystalline structure and purity were identified by X-ray diffraction (BrukerD8 Advance X-ray diffractometer in a Bragg-Brentano configuration, Karlsruhe, Germany) with Cu K $\alpha$ 1 and Cu K $\alpha$ 2 radiation. The morphologies and element distribution of particles were characterized by scanning electron microscopy (SEM, JSM-5600LV, JEOL, Tokyo, Japan) and high-resolution transmission electron microscopy (TEM, H-800, Hitachi, Tokyo, Japan).

### 2.3. Electrochemical Measurements

For the cathode preparation, cathode film was fabricated from a mixture consisting of 80 wt % active material, 10 wt % acetylene black, and 10 wt % polytetrafluoroethylene (PTFE). Then the film was cut into rounded slices, and dried at 120 °C overnight in a vacuum oven. Celgard 2400 polypropylene film (Charlotte, NC, USA) was used as separator. Ethylene carbonate/ethyl methyl carbonate/diethyl carbonate (EC:EMC:DEC = 1:1:1 by volume) solution containing 1 mol·L<sup>-1</sup> LiPF<sub>6</sub> was used as electrolyte. CR2032 coin-type test cells were assembled in an argon-filled glove box using Li foil as anode. The charge–discharge tests were carried out on a Land battery test system within a voltage range of 2–4.8 V vs. Li<sup>+</sup>/Li at room temperature. Electrochemical impedance spectrum (EIS) measurement was carried out on a CHI 660e electrochemical working station (Shanghai Chenhua Instrument Company, Shanghai, China).

## 3. Results and Discussion

### 3.1. Structures and Morphologies Characterization

Energy-dispersive X-ray spectroscopy (EDS) mapping was carried out to investigate the element distribution in the prepared precursor. As can be observed from Figure 1, Ni<sup>2+</sup> and Mn<sup>2+</sup> ions are distributed homogeneously. As shown in Figure 2, TG and DSC were used to identify the sintering temperature. The mass loss from 100 to 200 °C can be attributed to the loss of free water and crystal water from the precursor. Later, a rapid mass loss took place from 320 to 380 °C, with a sharp exothermic peak on the DSC curve. This process is corresponding to the decomposition of precursor in air and formation of preliminary particles. The last mass loss occurred from 380 to 600 °C and no obvious mass loss was observed after 600 °C. The crystallization process of layered Li-rich material may begin from about 350 °C and end at about 600 °C. Based on the above identifications, we sintered the precursor at 650, 750, 850, and 950 °C for 10 h, to optimize the synthesis temperature.

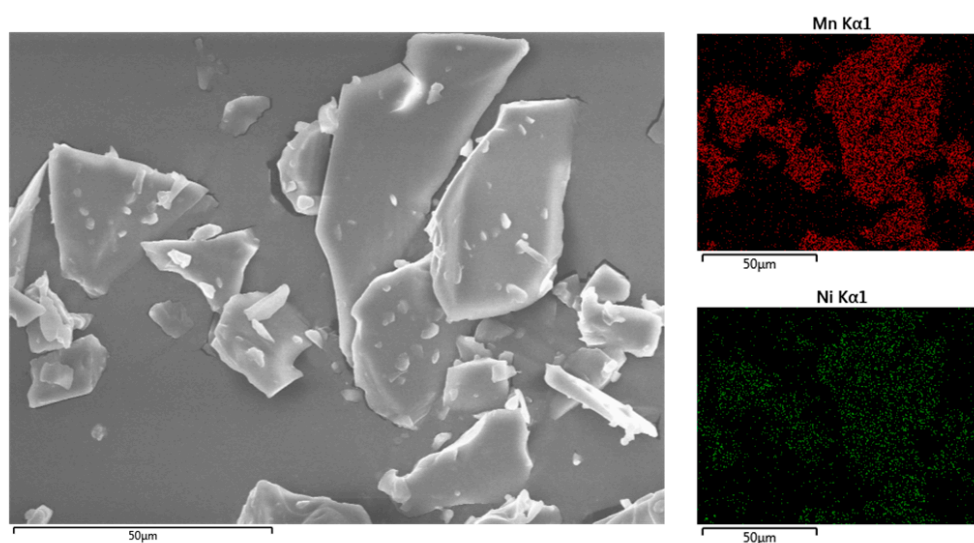
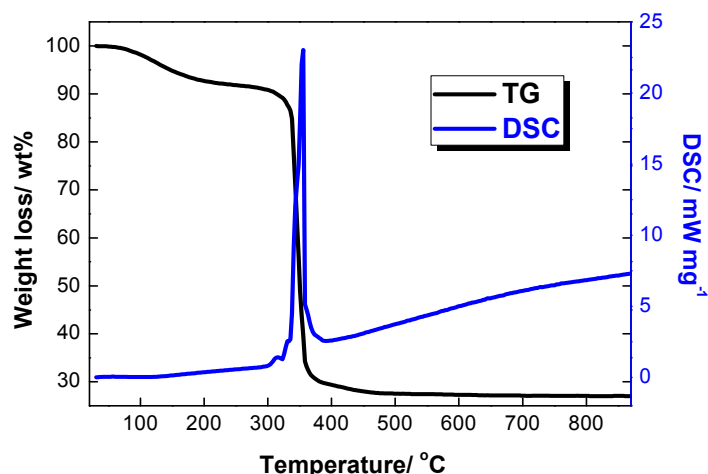
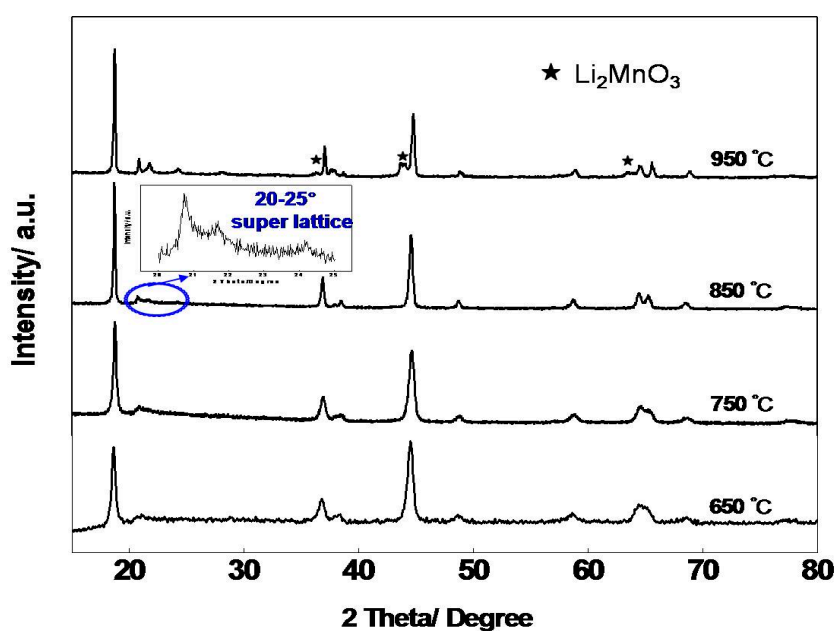


Figure 1. EDS mapping of the precursor.



**Figure 2.** Thermo-gravimetric (TG) and DSC curves for the precursor composite at a heating rate of  $4\text{ }^{\circ}\text{C}\cdot\text{min}^{-1}$  in flowing air.

Figure 3 shows the X-ray diffraction (XRD) patterns of  $\text{Li}_{1.2}\text{Mn}_{0.6}\text{Ni}_{0.2}\text{O}_2$  samples prepared at  $650\text{ }^{\circ}\text{C}$ ,  $750\text{ }^{\circ}\text{C}$ ,  $850\text{ }^{\circ}\text{C}$ , and  $950\text{ }^{\circ}\text{C}$  for 10 h. We can see that samples sintered at  $650\text{ }^{\circ}\text{C}$ ,  $750\text{ }^{\circ}\text{C}$ , and  $850\text{ }^{\circ}\text{C}$  are all indexed well in a hexagonal  $\alpha\text{-NaFeO}_2$  structure, and no other impurity phase is detected [42]. With increasing sintering temperature, the intensity of the peaks increases while the full width at half-maximum (FWHM) of the reflection decreases, which means that the crystallinity of samples become higher and the crystallites grow larger. However, the sample heated at  $950\text{ }^{\circ}\text{C}$  for 10 h is accompanied by  $\text{Li}_2\text{MnO}_3$  impurity. This means that at high temperatures such as  $950\text{ }^{\circ}\text{C}$ , Li-rich material is thermodynamically unstable, and preparation of layered Li-rich materials using the amorphous complex method is prone to phase segregation. Superstructure peaks around  $2\theta = 20^{\circ}\text{--}25^{\circ}$  results from ordering of the lithium ions and transition metal ions in the transition metal layer [43]. Furthermore, the splitting reflection peaks corresponding to (006)/(102) and (108)/(110) peak pairs are apparent for samples sintered above  $750\text{ }^{\circ}\text{C}$ , indicating layered structure is well-formed.



**Figure 3.** X-ray diffraction (XRD) patterns for the  $\text{Li}_{1.2}\text{Mn}_{0.6}\text{Ni}_{0.2}\text{O}_2$  samples prepared at  $650\text{ }^{\circ}\text{C}$ ,  $750\text{ }^{\circ}\text{C}$ ,  $850\text{ }^{\circ}\text{C}$ , and  $950\text{ }^{\circ}\text{C}$  for 10 h.

Since the radius of  $\text{Ni}^{2+}$  (0.69 Å) is similar to that of  $\text{Li}^+$  (0.76 Å), cation disorder may occur between  $\text{Ni}^{2+}$  and  $\text{Li}^+$  which may hinder  $\text{Li}^+$  intercalation/deintercalation during the charge/discharge process, which is harmful to material's electrochemical performances, especially rate capability. According to previous reports, intensity ratio in XRD profile  $I(003)/I(104)$  generally reflects  $\text{Li}^+/\text{Ni}^{2+}$  disorder, and a higher value means less cation mixing [44]. Moreover, the intensity ratio  $(I(006) + I(102))/I(101)$  can also indicate the hexagonal ordering, and a lower value means higher ordering [45]. The calculation results are shown in Table 1. We can see that when sintering temperature increased from 650 to 850 °C, the value of  $I(003)/I(104)$  ratio increased from 0.92 to 1.64;  $(I(006) + I(102))/I(101)$  is calculated as 0.38, which also represents an ordered layer structure. According to the above results, the nano-sized  $\text{Li}_{1.2}\text{Mn}_{0.6}\text{Ni}_{0.2}\text{O}_2$  samples sintered at 850 °C have a well-formed hexagonal layer structure and less  $\text{Li}^+/\text{Ni}^{2+}$  disorder, which may exhibit better electrochemical performances, especially rate capability.

**Table 1.** The values of  $I(003)/I(104)$  and  $(I(006) + I(102))/I(101)$  calculated from XRD patterns.

Sample	$I(003)/I(104)$	$(I(006) + I(102))/I(101)$
650 °C	0.92	0.60
750 °C	1.33	0.50
850 °C	1.64	0.41
950 °C	1.78	0.36

Figure 4 shows the morphologies for the samples sintered at 650–950 °C for 10 h. All the samples sintered at 650–950 °C are nanoparticles. For the samples sintered at 650 °C and 750 °C, nanoparticles with a size of about 100 nm are accompanied by formless parts. For the samples sintered at 850 °C, a morphology of well distributed nanoparticles is formed and the average particle size is about 200 nm. When the sintering temperature increases to 950 °C, the particles grow even bigger with some agglomeration to form a network, which agrees well with analysis of XRD patterns.

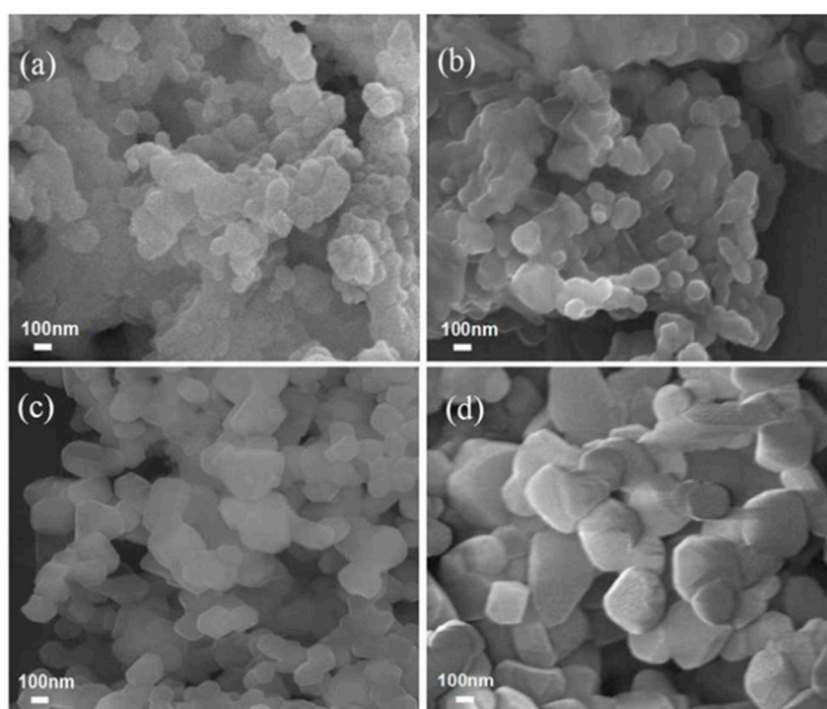


**Figure 4.** SEM images for the  $\text{Li}_{1.2}\text{Mn}_{0.6}\text{Ni}_{0.2}\text{O}_2$  samples sintered at different temperature: (a) 650 °C; (b) 750 °C; (c) 850 °C; and (d) 950 °C for 10 h.

Layered Li-rich materials are always synthesized under high temperatures (above 850 °C) for co-precipitation [42] and sol-gel preparation [25], because a lithium diffusion process is essential. However, it was reported that Ni ions prefer to be segregated near the particle surface during high temperature sintering in these synthesis processes, which might have negative effect on cycling stability and rate capability [33]. The amorphous complex method has been reported to be efficient in preparing nano-sized oxides at lower temperatures [37]. As shown in Figure 3, it can be clearly seen that layered structure material was obtained under 750 °C for 10 h, although its layered structure was not well-formed. We prolonged sintering time to 30 h under 750 °C, intending to investigate the practicality to synthesis layered Li-rich materials at lower temperatures. As shown in Figure 5a, after calcination at 750 °C for 30 h, the intensity of XRD peaks and typical splitting reflection peaks change little. Moreover, the calculation results of  $I(003)/I(104)$  and  $(I(006) + I(102))/I(101)$  are shown in Table 2, which also show little improvement. Figure 5b shows the morphology for the samples sintered at 750 °C for 30 h, which is still nanoparticles accompanied by formless parts, compared with the sample sintered at 750 °C for 10 h. Hence, it is clear that the calcination temperature of 750 °C is not sufficient for good hexagonal structure and nano-sized particle growth in the amorphous complex process.

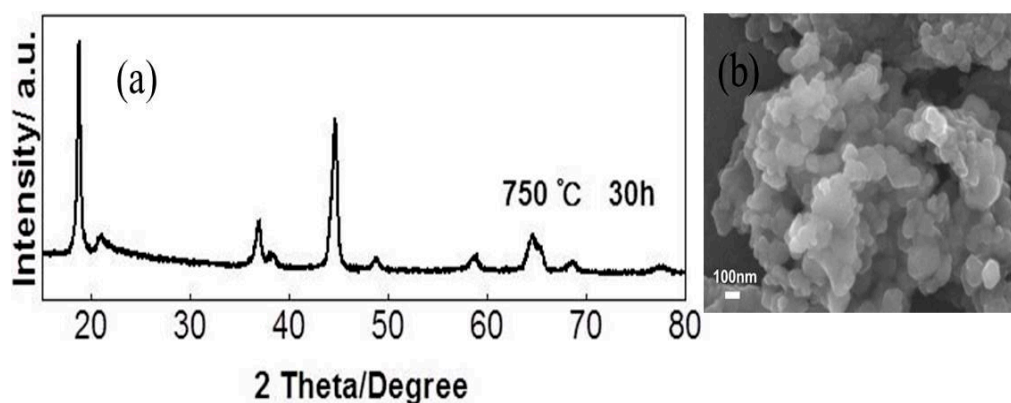
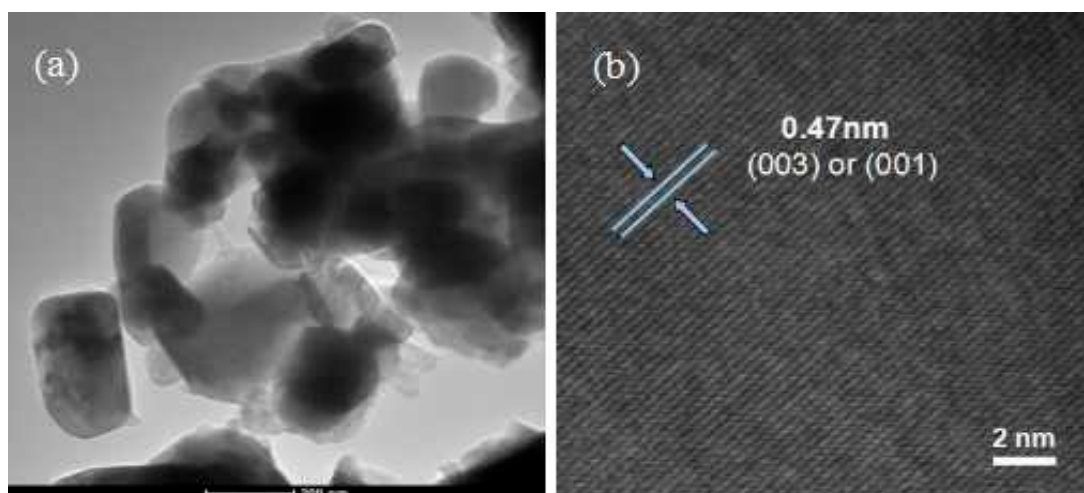


Figure 5. (a) XRD patterns; (b) SEM images for the  $\text{Li}_{1.2}\text{Mn}_{0.6}\text{Ni}_{0.2}\text{O}_2$  sample prepared at 750 °C for 30 h.

Table 2.  $I(003)/I(104)$  and  $(I(006) + I(102))/I(101)$  for sample sintered at 750 °C for 30 h.

Sample	$I(003)/I(104)$	$(I(006) + I(102))/I(101)$
750 °C for 30 h	1.34	0.52

Microstructure of the sample sintered at 850 °C was further investigated by EDS mapping, TEM and high-resolution TEM (HRTEM). As can be clearly seen from EDS mapping spectra (Supplementary Figure S1), Mn/Ni cations are uniformly distributed in the final product. The TEM image (Figure 6a) clearly shows that sample sintered at 850 °C consists of well distributed nanoparticles with an average size of 200 nm. The fringes in HRTEM image (Figure 6b) are identified as being 0.47 nm, which agrees well with the {003} and {001} lattice spacing of rhombohedral  $\text{LiMO}_2$  ( $M = \text{Mn}, \text{Ni}, \text{etc.}$ ). This means that the  $\text{Li}_{1.2}\text{Mn}_{0.6}\text{Ni}_{0.2}\text{O}_2$  samples sintered at 850 °C for 10 h are well-crystallized and well mono-dispersed single phase nanoparticles.



**Figure 6.** TEM (a) and high-resolution TEM (HRTEM); (b) images for the  $\text{Li}_{1.2}\text{Mn}_{0.6}\text{Ni}_{0.2}\text{O}_2$  samples sintered at  $850^\circ\text{C}$  for 10 h.

### 3.2. Electrochemical Performances of $\text{Li}_{1.2}\text{Mn}_{0.6}\text{Ni}_{0.2}\text{O}_2$ Material

Electrochemical performances of the samples prepared at different temperature are depicted in Figure 7. Figure 7a shows the charge/discharge profiles of the first cycle between 2.0 and 4.8 V vs.  $\text{Li}^+/\text{Li}$  at a current density of  $20\text{ mA}\cdot\text{g}^{-1}$ . The first region below 4.5 V is ascribed to the oxidation of  $\text{Ni}^{2+}$  to  $\text{Ni}^{4+}$ , while the subsequent flat region is assigned to the removal of  $\text{Li}_2\text{O}$  from such solid solution materials [13,42].

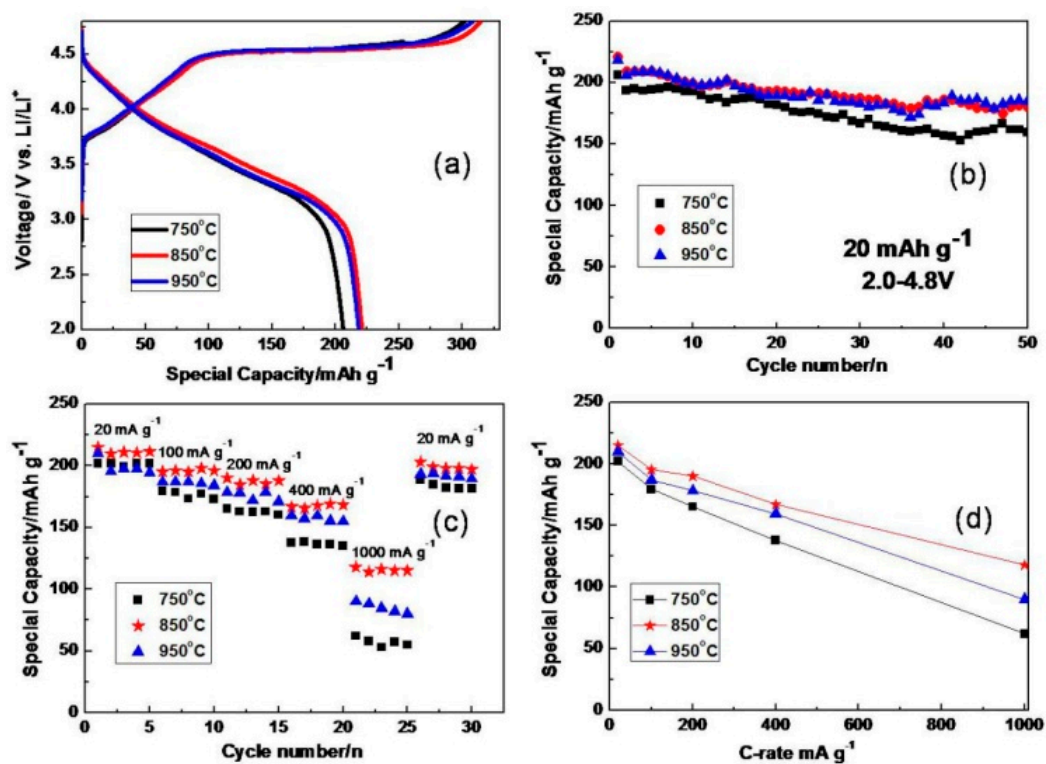


**Figure 7.** (a) Initial charge–discharge profiles at a current density of  $20\text{ mA}\cdot\text{g}^{-1}$ ; (b) cycling performance at a current density of  $20\text{ mA}\cdot\text{g}^{-1}$ ; (c) rate capability; and (d) comparison of discharge capacity at different rate.

The initial charge and discharge capacities for the sample prepared at 750 °C are measured as 306 mAh·g<sup>-1</sup> and 206 mAh·g<sup>-1</sup>, respectively. After 50 cycles, the discharge capacity retains at 159 mAh·g<sup>-1</sup> with the lowest capacity retention of 77.4%, which means its layered structure is not so stable. For the sample sintered at 850 °C, it delivers the highest initial discharge capacity of 221 mAh·g<sup>-1</sup>, which decreases to 180 mAh·g<sup>-1</sup> after 50 cycles with a retention of 81%. The initial discharge capacity of material synthesized at 950 °C is 218 mAh·g<sup>-1</sup>, which is slightly lower than that of sample prepared at 850 °C. However, it exhibits a higher capacity retention of 84% after 50 cycles. The main reason for capacity fading might also be the layer to spinel phase transformation, which we have mentioned before [19,20]. We have found that there is Li<sub>2</sub>MnO<sub>3</sub> phase separation for material synthesized at 950 °C, and nano-sized Li<sub>2</sub>MnO<sub>3</sub> with high crystallinity is reported to be slowly activated and exhibit somewhat stable discharge capacities at low current density [46,47], which maybe the main reason for its slightly lower initial discharge capacity.

Furthermore, to investigate the effect on kinetic behavior by reducing particle size to nanoscale, we investigated the rate capability of as-prepared samples at different current densities from 20 to 1000 mA·g<sup>-1</sup>. As compared in Figure 7c, the sample obtained at 850 °C shows the best rate performance. When the current density is increased to 200 mA·g<sup>-1</sup>, the capacity is as high as 190 mAh·g<sup>-1</sup>. Even when the discharge current density is increased up to 1000 mA·g<sup>-1</sup>, the capacity still can retain up to 118 mAh·g<sup>-1</sup>. Compared with some reported Li<sub>1.2</sub>Mn<sub>0.6</sub>Ni<sub>0.2</sub>O<sub>2</sub> materials without doping [48,49], the uniform nano-sized Li<sub>1.2</sub>Mn<sub>0.6</sub>Ni<sub>0.2</sub>O<sub>2</sub> material prepared by the amorphous complex method shows improved rate capability, which shows the benefits of reducing particle size for improving high rate performances of Li-rich materials.

It is apparent from Figure 7d that sintering temperature influences the rate capability significantly. Considering the analysis results of XRD and SEM, the relatively low temperature of 750 °C will bring about worse crystallinity and poor structure, which will have a negative impact on Li<sup>+</sup> insertion/extraction. While a high temperature of 950 °C may result in large particle size and Li<sub>2</sub>MnO<sub>3</sub> phase segregation, the sample obtained at 850 °C shows the best crystal structure features and uniform morphology, which leads to enhanced rate capability. To better understand electrochemical properties of the materials obtained at different temperatures, EIS measurements of these three samples were conducted.

Figure 8 shows Nyquist plots of fresh cells at open circuit voltages (OCV) at room temperature, right after the half-cell was assembled. All the Nyquist plots are composed of one semicircle and an inclined line. The semicircle at high frequency might be due to the R<sub>s</sub> (solid electrolyte interface resistance) and R<sub>ct</sub> (charge transfer resistance), and the inclined line at low frequency is attributed to Warburg impedance that is associated with Li<sup>+</sup> diffusion through the cathode. R<sub>s</sub> and R<sub>ct</sub> can sometimes overlap, especially when the cell was not cycled [50]. For these fresh cells without cycling, the solid electrolyte interface (SEI) formation is very weak and the semicircle is mainly determined by R<sub>ct</sub>. As seen in Figure 8, the R<sub>ct</sub> of material sintered at 850 °C (355 Ω) is smaller than that obtained from samples sintered at 750 °C (468 Ω) and 950 °C (390 Ω), which is indicative of higher electrical conductivity and faster electrochemical reactions [51]. We also evaluated the Li<sup>+</sup> diffusion coefficient at fully charged from EIS spectra using a reported method [52,53]. The results reveal that material sintered at 850 °C has a higher Li<sup>+</sup> diffusion coefficient (7.64 × 10<sup>-13</sup> cm<sup>2</sup>·s<sup>-1</sup>) than samples sintered at 750 °C (3.24 × 10<sup>-14</sup> cm<sup>2</sup>·s<sup>-1</sup>) and 950 °C (1.06 × 10<sup>-13</sup> cm<sup>2</sup>·s<sup>-1</sup>), which may be attributed to the uniform nano-sized distribution and lower Li<sup>+</sup>/Ni<sup>2+</sup> disorder of material sintered at 850 °C. As for material sintered at 950 °C, although its R<sub>ct</sub> is only slightly greater than that of the material sintered at 850 °C, it is well known that the Li<sup>+</sup> diffusion in Li<sub>2</sub>MnO<sub>3</sub> phase is slow, and the SEM image shows that the particle size is growing even bigger, which is predicted to have a negative impact on rate capability. Overall, the EIS testing results show that sample sintered an appropriate temperature of 850 °C shows the highest electrical conductivity and rapid Li<sup>+</sup> diffusion. The rapid Li<sup>+</sup> diffusion might be responsible for its enhanced rate capability.

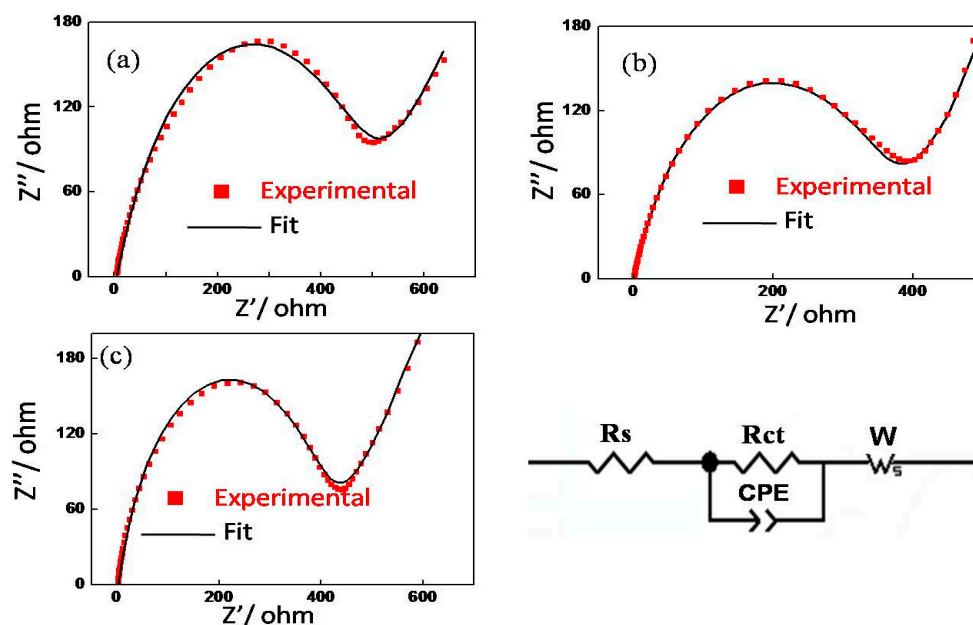


Figure 8. Nyquist plots of fresh cells of material sintered at (a) 750 °C; (b) 850 °C; and (c) 950 °C for 10 h.

#### 4. Conclusions

Well-dispersed  $\text{Li}_{1.2}\text{Ni}_{0.2}\text{Mn}_{0.6}\text{O}_2$  nanoparticles with an average size of 200 nm have been prepared by a facile amorphous complex method, and the influence of sintering temperature on crystallization using an amorphous complex precursor has been studied. The relatively low temperature of 750 °C is not sufficient for obtaining well-formed hexagonal ordering and nanoparticles' growth, while phase segregation may occur under high temperature as 950 °C, which indicates the thermodynamic instability of Li-rich materials at high temperature. The sample obtained at a sintering temperature of 850 °C shows uniform Mn/Ni cation distribution, good cycle ability, and rate capability, which maybe due to its good crystal structure and well-distributed nano morphology. This nano-sized material can deliver a capacity of  $221 \text{ mAh}\cdot\text{g}^{-1}$  at a current density of  $20 \text{ mA}\cdot\text{g}^{-1}$  in the potential window of 2.0–4.8 V vs.  $\text{Li}^+/\text{Li}$ , and remains about 81% after 50 cycles. The discharge capacity can be retained as high as  $118 \text{ mAh}\cdot\text{g}^{-1}$  even at a current density of  $1000 \text{ mA}\cdot\text{g}^{-1}$ . This study demonstrates a simple and efficient way to prepare nano-sized layered Li-rich cathode materials and shows the relationship between crystal structure and synthesis temperature. Although the as-prepared nano-sized sample sintered at 850 °C exhibits good crystal structure, uniform Mn/Ni cation distribution and improved kinetic behaviors, capacity fading still exists. Future work will be conducted to further understand the capacity fading mechanism, and use cation doping to improve its cycling stability and rate capability for further application in lithium-ion batteries.

**Supplementary Materials:** The following are available online at [www.mdpi.com/1996-1944/9/8/661/s1](http://www.mdpi.com/1996-1944/9/8/661/s1).

**Acknowledgments:** This work is supported by the Ministry of Science and Technology (MOST) (Grant No. 2013CB934000, No. 2014DFG71590), Beijing Municipal Program (Grant No. YETP0157).

**Author Contributions:** Xiangming He and Jixian Wang conceived and designed the experiments; Jixian Wang performed the experiments; Jixian Wang and Li Wang analyzed the data; All authors approved this manuscript.

**Conflicts of Interest:** The authors declare no conflict of interest.

## References

1. Tarascon, J.M.; Armand, M. Issues and challenges facing rechargeable lithium batteries. *Nature* **2001**, *414*, 359–367. [[CrossRef](#)] [[PubMed](#)]
2. Whittingham, M.S. Lithium Batteries and Cathode Materials. *Chem. Rev.* **2004**, *104*, 4271–4302. [[CrossRef](#)] [[PubMed](#)]
3. Chen, J. Recent Progress in Advanced Materials for Lithium Ion Batteries. *Materials* **2013**, *6*, 156–183. [[CrossRef](#)]
4. Wang, L.; He, X.; Li, J.; Sun, W.; Gao, J.; Guo, J.; Jiang, C. Nano-Structured Phosphorus Composite as High-Capacity Anode Materials for Lithium Batteries. *Angew. Chem. Int. Ed.* **2012**, *51*, 9034–9037. [[CrossRef](#)] [[PubMed](#)]
5. Goodenough, J.B. Evolution of Strategies for Modern Rechargeable Batteries. *Acc. Chem. Res.* **2013**, *46*, 1053–1061. [[CrossRef](#)] [[PubMed](#)]
6. Zhang, K.; Han, X.; Hu, Z.; Zhang, X.; Tao, Z.; Chen, J. Nanostructured Mn-based oxides for electrochemical energy storage and conversion. *Chem. Soc. Rev.* **2015**, *44*, 699–728. [[CrossRef](#)] [[PubMed](#)]
7. Kim, D.K.; Muralidharan, P.; Lee, H.W.; Ruffo, R.; Yang, Y.; Chan, C.K.; Peng, H.; Huggins, R.A.; Cui, Y. Spinel  $\text{LiMn}_2\text{O}_4$  Nanorods as Lithium Ion Battery Cathodes. *Nano Lett.* **2008**, *8*, 3948–3952. [[CrossRef](#)] [[PubMed](#)]
8. Johnson, C.S.; Kim, J.S.; Lefief, C.; Li, N.; Vaughey, J.T.; Thackeray, M.M. The significance of the  $\text{Li}_2\text{MnO}_3$  component in ‘composite’  $x\text{Li}_2\text{MnO}_3 (1 - x)\text{LiMn}_{0.5}\text{Ni}_{0.5}\text{O}_2$  electrodes. *Electrochem. Commun.* **2004**, *6*, 1085–1091. [[CrossRef](#)]
9. Koenig, G.M.; Belharouak, I.; Deng, H.; Sun, Y.K.; Amine, K. Composition-Tailored Synthesis of Gradient Transition Metal Precursor Particles for Lithium-Ion Battery Cathode Materials. *Chem. Mater.* **2011**, *23*, 1954–1963. [[CrossRef](#)]
10. Wang, F.; Chang, Z.; Wang, X.; Wang, Y.; Chen, B.; Zhu, Y.; Wu, Y. Composites of porous  $\text{Co}_3\text{O}_4$  grown on  $\text{Li}_2\text{MnO}_3$  microspheres as cathode materials for lithium ion batteries. *J. Mater. Chem. A* **2015**, *3*, 4840–4845. [[CrossRef](#)]
11. Martha, S.K.; Nanda, J.; Kim, Y.; Unocic, R.R.; Pannala, S.; Dudney, N.J. Solid electrolyte coated high voltage layered-layered lithium-rich composite cathode:  $\text{Li}_{1.2}\text{Mn}_{0.525}\text{Ni}_{0.175}\text{Co}_{0.1}\text{O}_2$ . *J. Mater. Chem. A* **2013**, *1*, 5587–5595. [[CrossRef](#)]
12. Li, Z.; Chernova, N.A.; Feng, J.; Upreti, S.; Omenya, F.; Whittingham, M.S. Stability and Rate Capability of Al Substituted Lithium-Rich High-Manganese Content Oxide Materials for Li-Ion Batteries. *J. Electrochem. Soc.* **2011**, *159*, A116–A120. [[CrossRef](#)]
13. Armstrong, A.R.; Holzapfel, M.; Novák, P.; Johnson, C.S.; Kang, S.H.; Thackeray, M.M.; Bruce, P.G. Demonstrating Oxygen Loss and Associated Structural Reorganization in the Lithium Battery Cathode  $\text{Li}[\text{Ni}_{0.2}\text{Li}_{0.2}\text{Mn}_{0.6}]\text{O}_2$ . *J. Am. Chem. Soc.* **2006**, *128*, 8694–8698. [[CrossRef](#)] [[PubMed](#)]
14. Thackeray, M.M.; Kang, S.H.; Johnson, C.S.; Vaughey, J.T.; Benedek, R.; Hackney, S.A.  $\text{Li}_2\text{MnO}_3$ -stabilized  $\text{LiMO}_2$  (M = Mn, Ni, Co) electrodes for lithium-ion batteries. *J. Mater. Chem.* **2007**, *17*, 3112–3125. [[CrossRef](#)]
15. Jarvis, K.A.; Deng, Z.; Allard, L.F.; Manthiram, A.; Ferreira, P.J. Atomic Structure of a Lithium-Rich Layered Oxide Material for Lithium-Ion Batteries: Evidence of a Solid Solution. *Chem. Mater.* **2011**, *23*, 3614–3621. [[CrossRef](#)]
16. Wang, J.; Yao, X.; Zhou, X.; Liu, Z. Synthesis and electrochemical properties of layered lithium transition metal oxides. *J. Mater. Chem.* **2011**, *21*, 2544–2549. [[CrossRef](#)]
17. Hong, J.; Seo, D.H.; Kim, S.W.; Gwon, H.; Oh, S.T.; Kang, K. Structural evolution of layered  $\text{Li}_{1.2}\text{Ni}_{0.2}\text{Mn}_{0.6}\text{O}_2$  upon electrochemical cycling in a Li rechargeable battery. *J. Mater. Chem.* **2010**, *20*, 10179–10186. [[CrossRef](#)]
18. Bareño, J.; Lei, C.H.; Wen, J.G.; Kang, S.H.; Petrov, I.; Abraham, D.P. Local Structure of Layered Oxide Electrode Materials for Lithium-Ion Batteries. *Adv. Mater.* **2010**, *22*, 1122–1127. [[CrossRef](#)] [[PubMed](#)]
19. Ito, A.; Shoda, K.; Sato, Y.; Hatano, M.; Horie, H.; Ohsawa, Y. Direct observation of the partial formation of a framework structure for Li-rich layered cathode material  $\text{Li}[\text{Ni}_{0.17}\text{Li}_{0.2}\text{Co}_{0.07}\text{Mn}_{0.56}]\text{O}_2$  upon the first charge and discharge. *J. Power Sources* **2011**, *196*, 4785–4790. [[CrossRef](#)]
20. Xu, B.; Fell, C.R.; Chi, M.; Meng, Y.S. Identifying surface structural changes in layered Li-excess nickel manganese oxides in high voltage lithium ion batteries: A joint experimental and theoretical study. *Energy Environ. Sci.* **2011**, *4*, 2223–2233. [[CrossRef](#)]

21. Lu, Z.; Chen, Z.; Dahn, J.R. Lack of Cation Clustering in  $\text{Li}[\text{Ni}_x\text{Li}_{1/3-2x/3}\text{Mn}_{2/3-x/3}]\text{O}_2$  ( $0 < x \leq 1/2$ ) and  $\text{Li}[\text{Cr}_x\text{Li}_{(1-x)/3}\text{Mn}_{(2-2x)/3}]\text{O}_2$  ( $0 < x < 1$ ). *Chem. Mater.* **2003**, *15*, 3214–3220.
22. Thackeray, M.M.; Kang, S.H.; Johnson, C.S.; Vaughey, J.T.; Hackney, S.A. Comments on the structural complexity of lithium-rich  $\text{Li}_{1+x}\text{M}_{1-x}\text{O}_2$  electrodes (M = Mn, Ni, Co) for lithium batteries. *Electrochem. Commun.* **2006**, *8*, 1531–1538. [[CrossRef](#)]
23. Wang, C.C.; Jarvis, K.A.; Ferreira, P.J.; Manthiram, A. Effect of Synthesis Conditions on the First Charge and Reversible Capacities of Lithium-Rich Layered Oxide Cathodes. *Chem. Mater.* **2013**, *25*, 3267–3275. [[CrossRef](#)]
24. Yang, X.; Wang, X.; Wei, Q.; Shu, H.; Liu, L.; Yang, S.; Hu, B.; Song, Y.; Zou, G.; Hu, L.; et al. Synthesis and characterization of a Li-rich layered cathode material  $\text{Li}_{1.15}[(\text{Mn}_{1/3}\text{Ni}_{1/3}\text{Co}_{1/3})_{0.5}(\text{Ni}_{1/4}\text{Mn}_{3/4})_{0.5}]_{0.85}\text{O}_2$  with spherical core-shell structure. *J. Mater. Chem.* **2012**, *22*, 19666–19672. [[CrossRef](#)]
25. Kim, J.H.; Sun, Y.K. Electrochemical performance of  $\text{Li}[\text{Li}_x\text{Ni}_{(1-3x)/2}\text{Mn}_{(1+x)/2}]\text{O}_2$  cathode materials synthesized by a sol-gel method. *J. Power Sources* **2003**, *119–121*, 166–170. [[CrossRef](#)]
26. Lee, Y.; Kim, M.G.; Cho, J. Layered  $\text{Li}_{0.88}[\text{Li}_{0.18}\text{Co}_{0.33}\text{Mn}_{0.49}]\text{O}_2$  Nanowires for Fast and High Capacity Li-Ion Storage Material. *Nano Lett.* **2008**, *8*, 957–961. [[CrossRef](#)] [[PubMed](#)]
27. Park, Y.J.; Hong, Y.S.; Wu, X.; Ryu, K.S.; Chang, S.H. Structural investigation and electrochemical behaviour of  $\text{Li}[\text{Ni}_x\text{Li}_{(1/3-2x/3)}\text{Mn}_{(2/3-x/3)}]\text{O}_2$  compounds by a simple combustion method. *J. Power Sources* **2004**, *129*, 288–295. [[CrossRef](#)]
28. Cho, J.; Kim, Y.; Kim, M.G. Synthesis and Characterization of  $\text{Li}[\text{Ni}_{0.41}\text{Li}_{0.08}\text{Mn}_{0.51}]\text{O}_2$  Nanoplates for Li Battery Cathode Material. *J. Phys. Chem. C* **2007**, *111*, 3192–3196. [[CrossRef](#)]
29. Wei, G.Z.; Lu, X.; Ke, F.S.; Huang, L.; Li, J.T.; Wang, Z.X.; Zhou, Z.Y.; Sun, S.G. Crystal Habit-Tuned Nanoplate Material of  $\text{Li}[\text{Li}_{1/3-2x/3}\text{Ni}_x\text{Mn}_{2/3-x/3}]\text{O}_2$  for High-Rate Performance Lithium-Ion Batteries. *Adv. Mater.* **2010**, *22*, 4364–4367. [[CrossRef](#)] [[PubMed](#)]
30. Guo, Y.G.; Hu, J.S.; Wan, L.J. Nanostructured materials for electrochemical energy conversion and storage devices. *Adv. Mater.* **2008**, *20*, 2878–2887. [[CrossRef](#)]
31. Zheng, J.; Gu, M.; Genc, A.; Xiao, J.; Xu, P.; Chen, X.; Zhu, Z.; Zhao, W.; Pullan, L.; Wang, C.; et al. Mitigating Voltage Fade in Cathode Materials by Improving the Atomic Level Uniformity of Elemental Distribution. *Nano Lett.* **2014**, *14*, 2628–2635. [[CrossRef](#)] [[PubMed](#)]
32. Gu, M.; Belharouak, I.; Genc, A.; Wang, Z.; Wang, D.; Amine, K.; Gao, F.; Zhou, G.; Thevuthasan, S.; Baer, D.R.; et al. Conflicting Roles of Nickel in Controlling Cathode Performance in Lithium Ion Batteries. *Nano Lett.* **2012**, *12*, 5186–5191. [[CrossRef](#)] [[PubMed](#)]
33. Gu, M.; Genc, A.; Belharouak, I.; Wang, D.; Amine, K.; Thevuthasan, S.; Baer, D.R.; Zhang, J.G.; Browning, N.D.; Liu, J. Nanoscale phase separation, cation ordering, and surface chemistry in pristine  $\text{Li}_{1.2}\text{Ni}_{0.2}\text{Mn}_{0.6}\text{O}_2$  for Li-ion batteries. *Chem. Mater.* **2013**, *25*, 2319–2326. [[CrossRef](#)]
34. Gu, M.; Belharouak, I.; Zheng, J.; Wu, H.; Xiao, J.; Genc, A.; Amine, K.; Thevuthasan, S.; Baer, D.R.; Zhang, J.G. Formation of the spinel phase in the layered composite cathode used in Li-ion batteries. *ACS Nano* **2012**, *7*, 760–767. [[CrossRef](#)] [[PubMed](#)]
35. Battle, P.D.; Bell, A.M.T.; Blundell, S.J.; Coldea, A.I.; Cussen, E.J.; Hardy, G.C.; Marshall, I.M.; Rosseinsky, M.J.; Steer, C.A. Chemically Induced Magnetism and Magneto resistance in  $\text{La}_{0.8}\text{Sr}_{1.2}\text{Mn}_{0.6}\text{Rh}_{0.4}\text{O}_4$ . *J. Am. Chem. Soc.* **2001**, *123*, 7610–7615. [[CrossRef](#)] [[PubMed](#)]
36. García de la Cruz, R.M.; Falcón, H.; Peña, M.A.; Fierro, J.L.G. Role of bulk and surface structures of  $\text{La}_{1-x}\text{Sr}_x\text{NiO}_3$  perovskite-type oxides in methane combustion. *Appl. Catal. B Environ.* **2001**, *33*, 45–55. [[CrossRef](#)]
37. Zhu, Y.; Tan, R.; Yi, T.; Ji, S.; Ye, X.; Cao, L. Preparation of nanosized  $\text{LaCoO}_3$  perovskite oxide using amorphous heteronuclear complex as a precursor at low temperature. *J. Mater. Sci.* **2000**, *35*, 5415–5420. [[CrossRef](#)]
38. Gopukumar, S.; Chung, K.Y.; Kim, K.B. Novel synthesis of layered  $\text{LiNi}_{1/2}\text{Mn}_{1/2}\text{O}_2$  as cathode material for lithium rechargeable cells. *Electrochim. Acta* **2004**, *49*, 803–810. [[CrossRef](#)]
39. Zhang, S.; Zhang, C.; Man, Y.; Zhu, Y. Visible-light-driven photocatalyst of  $\text{Bi}_2\text{WO}_6$  nanoparticles prepared via amorphous complex precursor and photocatalytic properties. *J. Solid State Chem.* **2006**, *179*, 62–69. [[CrossRef](#)]
40. Zhu, Y.; Wang, H.; Tan, R.; Cao, L. Preparation of nanosized  $\text{La}_{1-x}\text{Sr}_x\text{CoO}_3$  via  $\text{La}_{1-x}\text{Sr}_x\text{Co}(\text{DTPA})\cdot 6\text{H}_2\text{O}$  amorphous complex precursor. *J. Alloys Compd.* **2003**, *352*, 134–139. [[CrossRef](#)]

41. Martinez-de La Cruz, A.; Villarreal, S.M.G.M.; Torres-Martínez, L.M.; Cuéllar, E.L.; Méndez, U.O. Photoassisted degradation of rhodamine B by nanoparticles of  $\alpha$ - $\text{Bi}_2\text{Mo}_3\text{O}_{12}$  prepared by an amorphous complex precursor. *Mater. Chem. Phys.* **2008**, *112*, 679–685. [[CrossRef](#)]
42. Lu, Z.; Dahn, J.R. Understanding the Anomalous Capacity of Li /  $\text{Li}[\text{Ni}_x\text{Li}_{(1/3-2x/3)}\text{Mn}_{(2/3-x/3)}]\text{O}_2$  Cells Using in Situ X-ray Diffraction and Electrochemical Studies. *J. Electrochem. Soc.* **2002**, *149*, A815–A822. [[CrossRef](#)]
43. Lim, J.H.; Bang, H.; Lee, K.S.; Amine, K.; Sun, Y.K. Electrochemical characterization of  $\text{Li}_2\text{MnO}_3$ – $\text{Li}[\text{Ni}_{1/3}\text{Co}_{1/3}\text{Mn}_{1/3}]\text{O}_2$ – $\text{LiNiO}_2$  cathode synthesized via co-precipitation for lithium secondary batteries. *J. Power Sources* **2009**, *189*, 571–575. [[CrossRef](#)]
44. Ohzuku, T.; Ueda, A.; Nagayama, M.; Iwakoshi, Y.; Komori, H. Comparative study of  $\text{LiCoO}_2$ ,  $\text{LiNi}_{1/2}\text{Co}_{1/2}\text{O}_2$  and  $\text{LiNiO}_2$  for 4 volt secondary lithium cells. *Electrochim. Acta* **1993**, *38*, 1159–1167. [[CrossRef](#)]
45. Sivaprakash, S.; Majumder, S.B.; Nieto, S.; Katiyar, R.S. Crystal chemistry modification of lithium nickel cobalt oxide cathodes for lithium ion rechargeable batteries. *J. Power Sources* **2007**, *170*, 433–440. [[CrossRef](#)]
46. Yu, D.Y.W.; Yanagida, K. Structural Analysis of  $\text{Li}_2\text{MnO}_3$  and Related Li-Mn-O Materials. *J. Electrochem. Soc.* **2011**, *158*, A1015–A1022. [[CrossRef](#)]
47. Lim, J.; Moon, J.; Gim, J.; Kim, S.; Kim, K.; Song, J.; Kang, J.; Im, W.B.; Kim, J. Fully activated  $\text{Li}_2\text{MnO}_3$  nanoparticles by oxidation reaction. *J. Mater. Chem.* **2012**, *22*, 11772–11777. [[CrossRef](#)]
48. Liu, X.; Huang, T.; Yu, A. Fe doped  $\text{Li}_{1.2}\text{Mn}_{0.6-x/2}\text{Ni}_{0.2-x/2}\text{Fe}_x\text{O}_2$  ( $x \leq 0.1$ ) as cathode materials for lithium-ion batteries. *Electrochim. Acta* **2014**, *133*, 555–563. [[CrossRef](#)]
49. Li, J.; Zhan, C.; Lu, J.; Yuan, Y.; Shahbazian-Yassar, R.; Qiu, X.; Amine, K. Improve First-Cycle Efficiency and Rate Performance of Layered-Layered  $\text{Li}_{1.2}\text{Mn}_{0.6}\text{Ni}_{0.2}\text{O}_2$  Using Oxygen Stabilizing Dopant. *ACS Appl. Mater. Interfaces* **2015**, *7*, 16040–16045. [[CrossRef](#)] [[PubMed](#)]
50. Ates, M.N.; Jia, Q.; Shah, A.; Busnaina, A.; Mukerjee, S.; Abraham, K.M. Mitigation of Layered to Spinel Conversion of a Li-Rich Layered Metal Oxide Cathode Material for Li-Ion Batteries. *J. Electrochem. Soc.* **2014**, *161*, A290–A301. [[CrossRef](#)]
51. Li, Y.; Bai, Y.; Bi, X.; Qian, J.; Ma, L.; Tian, J.; Wu, C.; Wu, F.; Lu, J.; Amine, K. An Effectively Activated Hierarchical Nano/Microspherical  $\text{Li}_{1.2}\text{Ni}_{0.2}\text{Mn}_{0.6}\text{O}_2$  Cathode for Long-Life and High-Rate Lithium-Ion Batteries. *ChemSusChem* **2016**, *9*, 728–735. [[CrossRef](#)] [[PubMed](#)]
52. Cao, Y.; Xiao, L.; Wang, W.; Choi, D.; Nie, Z.; Yu, J.; Saraf, L.V.; Yang, Z.; Liu, J. Reversible sodium ion insertion in single crystalline manganese oxide nanowires with long cycle life. *Adv. Mater.* **2011**, *23*, 3155–3160. [[CrossRef](#)] [[PubMed](#)]
53. Jafta, C.J.; Ozoemena, K.I.; Mathe, M.K.; Roos, W.D. Synthesis, characterisation and electrochemical intercalation kinetics of nanostructured aluminium-doped  $\text{Li}[\text{Li}_{0.2}\text{Mn}_{0.54}\text{Ni}_{0.13}\text{Co}_{0.13}]\text{O}_2$  cathode material for lithium ion battery. *Electrochim. Acta* **2012**, *85*, 411–422. [[CrossRef](#)]

